Journal of the Optical Society of Korea, Vol. 7, No. 1, March 2003, pp. 13-19

Stress Profile Dependence of the Optical Properties in Strained Quantum Wire Arrays

Jong Chang Yi* and Jeong-Beom Ji

School of Electronic and Electrical Engineering, Hong Ik University, Seoul 121-791, KOREA

(Received November 14, 2002)

The effects of strain distribution in quantum wire arrays have been analyzed using a finite-element method including both the hydrostatic and shear strain components. Their effects on the optical properties of the quantum wire arrays are assessed for various types of stress profiles by calculating the optical gain and the polarization dependence. The results show unique polarization dependency, which can be exploited either for the single polarization or the polarization-independent operation in quantum wire photonic devices.

OCIS codes : 160.6000, 230.5590, 140.5960.

I. INTRODUCTION

Research activity in the field of low-dimensional quantum structures, or nanostructures, continues to intensify, driven by the requirement for ever-shrinking microelectronic systems or by interesting physical phenomena. Among them the strained quantum wire structures, which provide strong quantum size effects as well as uniform size distribution, have undergone extensive study and development for their enhanced optical gain compared to the unstrained counterpart [1–4]. Obviously the main purpose of fabricating quantum wires is to generate semiconductor heterostructures with properties superior to quantum wells. The lateral superlattice is one of the most promising structures with its small size and higher wire density [5–7]. One drawback in it, however, is the relatively weak lateral confinement due to the lateral material intermixing [6,7]. Recent successes in the fabrication of the strained lateral superlattice quantum wire structures point to the possibility of additional lateral confinement due to the deformation potential [1,2]. In this paper, the effects of the strain distribution in the quantum wire arrays are analyzed using a linearized finite-element method [8,9] including both the hydrostatic and shear strain components. The effects of the strain on the band structures are modeled after Pikus and Bir [10,11]. The resulting optical properties in the strained and unstrained lateral superlattice quantum wires are compared between different types of stress profiles by calculating the optical gain and its polarization dependency [9,12,13].

II. STRESS PROFILES

In quantum well structures, there is only one type of strain profile: That is the uniaxial strain. Whereas, in the quantum wire structures, the strain profile can be uniaxial along either the lateral direction or the vertical direction. The strain can also be hydrostatic by surrounding the quantum wires with one material. Fig. 1 shows some of the possible stress types for the InGaAs quantum wires surrounded by the InAlGaAs materials.

The wire material is taken as $In_{0.3}Ga_{0.7}As$ and the surrounding materials are $Al_{0.4}Ga_{0.6}As$ *and/or* $In_{0.3}Al_{0.5}Ga_{0.2}As$. Table 1 shows the relevant material parameters for these three materials [14]. The $Al_{0.4}Ga_{0.6}As$ material has a smaller lattice constant and a larger bandgap energy than $In_{0.3}Ga_{0.7}As$, hence it provides both the compressive stress and the potential band offset. On the other hand, the $In_{0.3}Al_{0.5}Ga_{0.2}As$ material has a higher bandgap energy but almost the same lattice constant as the quantum wire material, so it provides only the potential band offset.

Typical strained quantum wire array is as shown in type B, where an InGaAs/InAlGaAs lateral superlattice is grown on AlGaAs substrate [15]. In that case

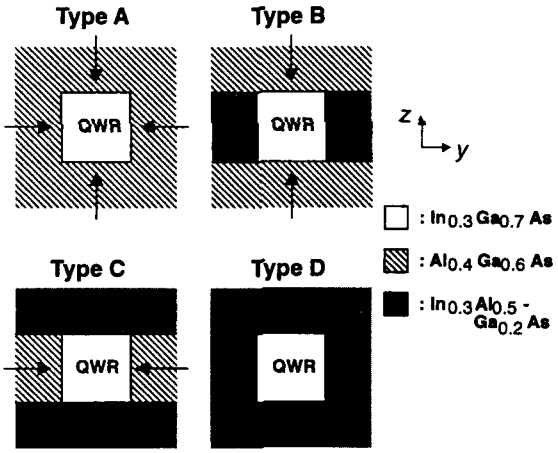

FIG. 1. Cross sectional profile of strained quantum wires. Arrows indicate the direction of stress. The $Al_{0.4}Ga_{0.6}As$ material provides both the compressive stress and the potential band offset. The $In_{0.3}Al_{0.5}$-$Ga_{0.2}As$ material has almost the same lattice constant as the $In_{0.3}Ga_{0.7}As$, so it only provides the potential band offset. Thus type A has the hydrostatic stress, type B has the uniaxial stress along the vertical direction, type C has the lateral stress, and type D has no stress.

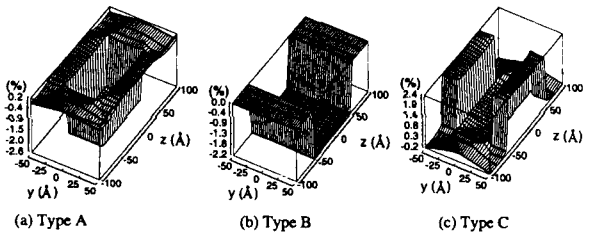

FIG. 2. Volume change in the various types of the strained quantum wire arrays shown in Fig. 1. Wire width and separation are 50 Å and wire height is 100 Å. The volume change reflects the hydrostatic strain profile since $\Delta V/V = \epsilon_{xx} + \epsilon_{yy} + \epsilon_{zz}$.

the stress is applied uniaxially along the vertical direction, as commonly happening in the strained quantum well structures. However, if one grows an InGaAs/AlGaAs lateral superlattice on AlGaAs substrate, the stress is from both directions as in type A [3]. Furthermore, if one uses InAlGaAs as the substrate material and grows InGaAs/AlGaAs lateral superlattice, the stress is along the lateral direction [2]. Therefore, one can expect laterally uniaxial strain in type C.

The actual lattice volume change profile for each type is calculated by an finite-element method [8] and is plotted in Fig. 2. The wire width and the wire separation are taken as 50 Å and the wire height is taken as 100 Å, which are close to the optimum quantum wire lateral dimensions. The volume change reflects the hydrostatic strain profile since $\Delta V/V = \epsilon_{xx} + \epsilon_{yy} + \epsilon_{zz}$. Type D has almost no lattice mismatch so it is an unstrained quantum wire array and its obvious strain profile is omitted in Fig. 2. The shear strain components are also calculated and included in the analysis of the band structures as outlined in the reference [8].

In type A, the wire material is compressed approximately 2.6 %. In type B, both the wires and barriers are compressed about 2.2 % and the strain is uniform along the lateral direction since the wire and barrier materials have almost the same lattice constants. In type C, the wire material is very slightly strained but the barrier material is expanded by approximately 2.4 %. In both type A and type C, there is a strong discontinuity in the strain profile along the lateral direction.

III. BAND STRUCTURES

The effects of the strain on the band structure are calculated by using the Pikus and Bir model [8]. Fig. 3 shows the corresponding band profiles along the horizontal direction at the center of the quantum wire. Types A-C are the strained quantum wire arrays and type D is the unstrained quantum wire array as illustrated in Fig. 1. In Fig. 3, C denotes the conduction band, and HH and LH denote the heavy hole and light hole bands, respectively. The dashed lines indicate the bulk band positions with no strain effect.

In type A, the conduction band shifts upwards, and the HH and LH bands split as they shift downwards, as in most compressively strained materials. In type B, the band change shows a similar trend with type A except that the band deformation is almost uniform

TABLE 1. Material parameters for InAlGaAs materials under investigation. The conduction and valence band offsets are estimated with respect to $In_{0.3}Ga_{0.7}As$ quantum wire material.

	$In_{0.3}Ga_{0.7}As$	$Al_{0.4}Ga_{0.6}As$	$In_{0.3}Al_{0.5}$-$Ga_{0.2}As$
Bandgap, Eg (eV)	1.019	1.966	1.948
lattice constant, a_o (Å) (lattice mismatch)	5.7748	5.6574 (−2.1 %)	5.7787 (0.006 %)
CB offset, E_c (eV)	0	0.663	0.576
VB offset, E_v (eV)	0	0.285	0.352

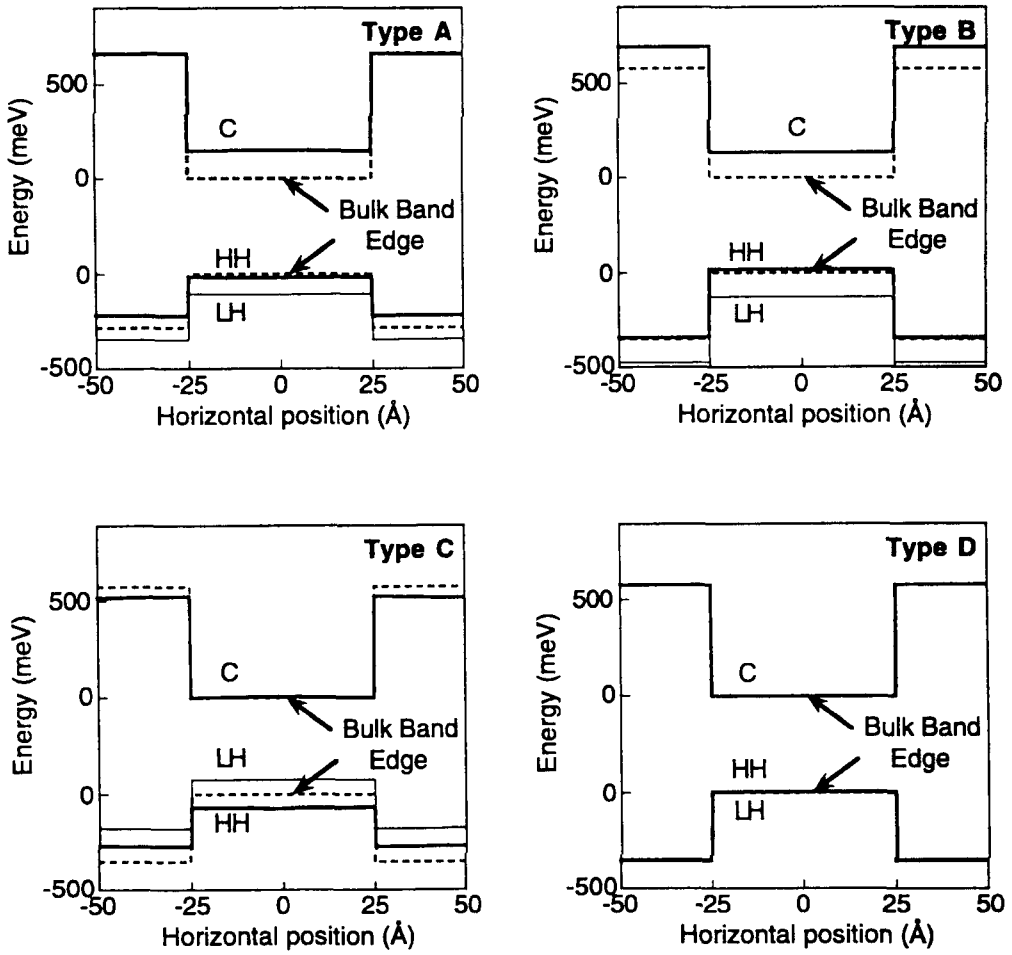

FIG. 3. Band profile along the horizontal direction at the center of the quantum wire in various types of the strained(A-C) and unstrained(D) quantum wire arrays shown in Fig. 1. C denotes the conduction band, and HH and LH denote the heavy hole and light hole bands, respectively. The dashed lines indicate the bulk band positions with no strain effect.

inside and outside the quantum wires. This is because the lattice constants of the quantum wire and barrier regions are almost the same. Fig. 3(c) shows the resulting band deformation in type C. In this case, the net volume change inside the quantum wire is very small hence the conduction band shift inside the quantum wire region is almost negligible.

However, the lattice constant of the barrier region is smaller than that of the quantum wire region in type C. Thus, its quantum wire regions will be suppressed vertically to match the smaller lattice constant of the barrier regions. The vertically suppressed quantum wire regions will eventually expand along the lateral direction to fill the barrier regions. As a result, the quantum wire regions will be suppressed vertically and expand along the lateral direction, which is quite similar to the quantum well with a tensile strain. Therefore, the LH band moves upwards and the HH band is suppressed downwards as shown in Fig. 3(c). When one compares type C to type A, one can find that the wires in type C has a geometric similarity to the barriers in type A, except that its lattice constant is larger than those of surrounding regions. The quantum wires of type C are lattice matched to the substrate and the barriers between them have a smaller lattice constant, while the barriers of type A are lattice matched to the substrate and the wires between them have a larger lattice constant. Thus, the strain coefficients in the quantum wires of type C would have the opposite signs from those in the barriers of type A. In Fig. 3(a), the HH band is higher than the LH band in the barrier regions of type A. Therefore, in type C, the LH band becomes higher than the HH band since the signs of the strain coefficients are reversed. The largest split energy between HH and LH bands among the four types is observed in type C and the second is in type B. It is almost twice as large as that in type A, not to mention the unstrained type D where the HH and LH bands are degenerate.

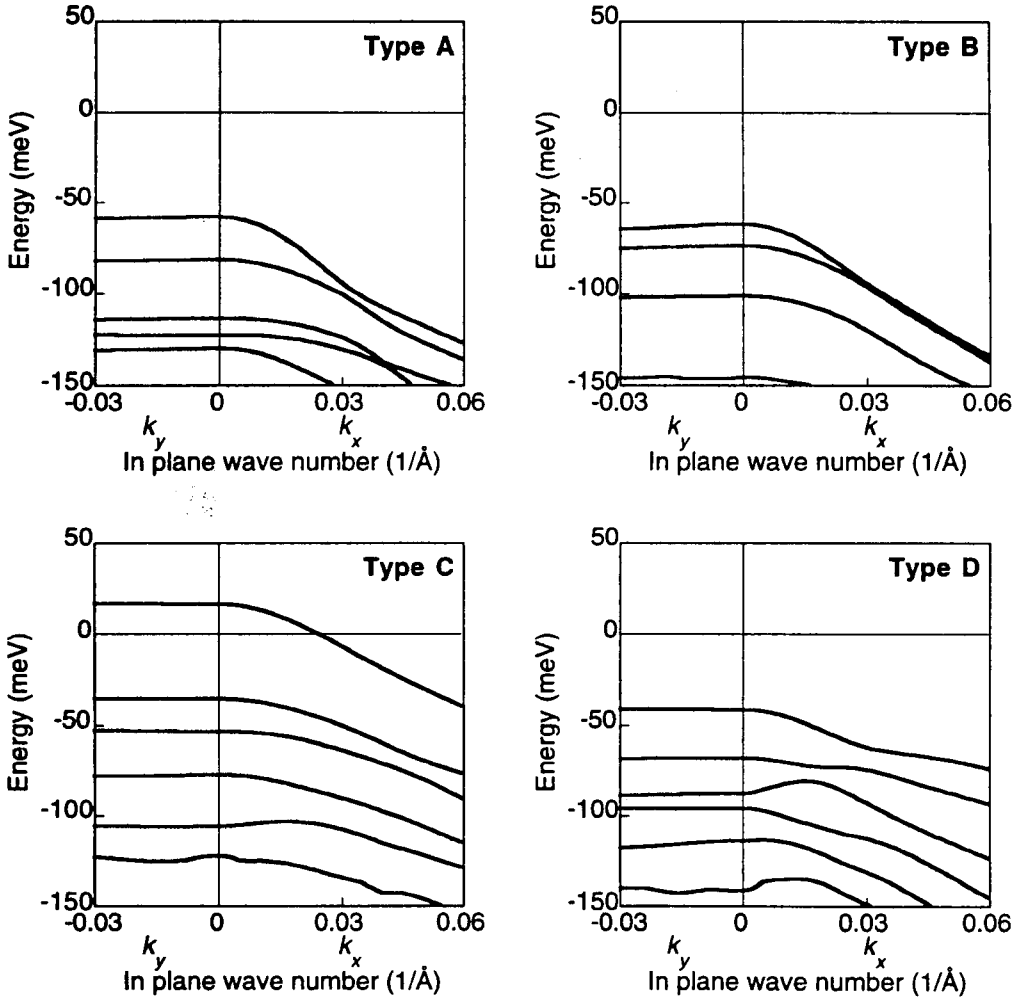

FIG. 4. Band diagrams of various types of the strained(A-C) and unstrained(D) quantum wire arrays shown in Fig. 3. Energy level is with respect to the top of the bulk valence band of $In_{0.3}Ga_{0.7}As$ with no strain effect. The quantum wires are parallel to the x-axis and are distributed along the y-axis.

Fig. 4 shows the actual subband energy dispersion diagram in the various types of the quantum wire arrays shown in Fig. 1. For simplicity, only the top valence band states up to 4 or 6 states are plotted. The zero level is the bulk valence band edge of the $In_{0.3}Ga_{0.7}As$ material with no strain effect. The x-axis is parallel to the wire axis and the y-axis is the lateral direction along which the quantum wire array is distributed. Along the array direction, the band dispersion is almost negligible due to the fairly high barrier potential height and the heavy valence band effective mass.

In types A through C, the energy dispersion along the wire axis is almost parabolic and they show little valence band intermixing. However, in type A, the HH-LH subband separation is about 86 meV. Thus, one can see a significant valence band intermixing at lower than that energy level. The energy splitting between the top two valence band states varies significantly from one type to another. They are approximately 23.0, 11.7, 52.1, and 26.6 meV for types A through D, respectively, as shown in Table 2. Type C has the largest value since the subbands are all LH-like so the effective mass is small. Whereas, type B has the smallest value since the subbands are dominantly HH-like. Types A and D would have effective masses in between types B and C.

Although one can estimate the effective masses of the valence subbands from the subband energy separation, it is only valid along the growth direction. The effective masses along the quantum wire axis, however, can be more accurately estimated from the second order derivatives of the energy dispersion along the quantum wire axis. Since Fig.4 has already shown the valence band energy dispersion along the wire axis, one can readily estimate the effective masses of each

TABLE 2. Band characteristics of the four types of quantum wire arrays shown in Fig. 1. E_c and E_v are the CB and VB band offsets, E_{HH}-E_{LH} is the HH-to-LH subband separation, m^*_{vx} is the in-plane effective mass of the top valence subband along the quantum wire axis, E_{v2}-E_{v1} is the subband energy gap between the top two valence subbands, and P_x, P_y, and P_z are the relative magnitudes of the momentum matrix elements along the x, y, and z polarizations.

	Type A	Type B	Type C	Type D
E_c (meV)	514	559	516	581
E_v(meV)	201	358	199	354
E_{HH}-E_{LH} (meV)	86	143	−147	−4
m^*_{vx} (m_0)	0.080	0.085	0.121	0.112
E_{v2}-E_{v1} (meV)	23.0	11.7	52.1	26.6
P_x: TE_x	0.60	0.56	0.41	0.55
P_y: TE_y	0.12	0.32	0.01	0.03
P_z: TM	0.19	0.04	0.49	0.32

subband from the second order derivatives of the energy dispersion. Table 2 shows the in-plane effective masses along the wire axis, m^*_{vx}, of the top valence subband in the four types of the quantum wire arrays. It clearly indicates that the in-plane effective mass of the LH-like subband in type C is heavier than that of the HH-like subband in type A or B. This phenomenon can be explained as follows. The uniaxially compressive stress along the vertical direction tends to induce the effective mass heavier along the vertical direct ion while it makes the effective mass lighter along the lateral direction, and vice versa for the tensile strain[10,16]. Therefore, in the HH-like subbands of types A and B, the increase in the effective masses along the growth direction would reduce the effective masses along the in-plane direction. On the other hand, in the LH-like subbands in type C, the decrease in the effective masses along the growth direction would make the in-plane effective masses heavier. Thus the valence band effective masses in the strained quantum wires would be strongly anisotropic and very hard to predict without comprehensive optical gain calculations [13].

IV. POLARIZATION DEPENDENCE

Due to the complicated nature of the valence band structure, it is quite difficult to tell whether a valence subband is heavy hole-like or light hole-like. Since its effective mass is strongly anisotropic and the subbands are usually strongly intermixed with adjacent subbands, it is almost impossible to determine from the band structure only. One of the best ways to judge the subband nature would be to characterize the polarization dependence of the dipole momentum matrix elements of the subband under consideration. Since both the optical gain and the PL intensity are proportional to the dipole momentum matrix element [13], the analysis of its polarization dependence will lead to overall gain anisotropy characterization. In typical quantum wires, the heavy hole-like subband would show the maximum dipole momentum when the electric field is polarized along the quantum wire axis. Whereas, the light hole-like subband would show the maximum dipole momentum when the electric field is polarized along the strongest lateral confinement direction. Fig. 5 shows the dipole momentum matrix elements in various types of quantum wire arrays as well as the optical gain for three different polarizations. Again, the x-axis is chosen to be parallel to the quantum wire axis, the y-axis along the lateral direction, and the z-axis along the growth direction, as shown in the diagram on the top of Fig. 5. The spherical plots of the dipole momentum matrix elements are all projected to the same perspective as in the top diagram. In the unstrained quantum wire array, the top valence band is mostly HH-like, so the dipole momentum becomes the strongest along the wire axis [13], as shown in Fig. 5(d). Thus, as shown on the right side of Fig. 5(d), the optical gain is maximum for the x-polarization as denoted by TE.x, while it is minimum for the y-polarization as denoted by TE.y. In the gain calculation, the energy broadening is taken as 7 meV and temperature as 300 K.

In case of type A, the dipole momentum is maximum along the TE.x polarization and so is the material gain. However, the overall shape of the dipole momentum is squeezed along the lateral and the vertical directions. In type B, where the stress is along the vertical direction, the shape of the dipole momentum is also squeezed along the vertical direction. Thus the optical gain for the TM polarization is almost negligible. In type C, where the stress is along the lateral direction, the shape of the dipole momentum is also squeezed along the lateral direction and is boosted along the vertical direction. Hence the material gain is maximum for the TM polarization. For this particular type of strain, the material gains for the TM and TE.x polarizations are almost the same, so one

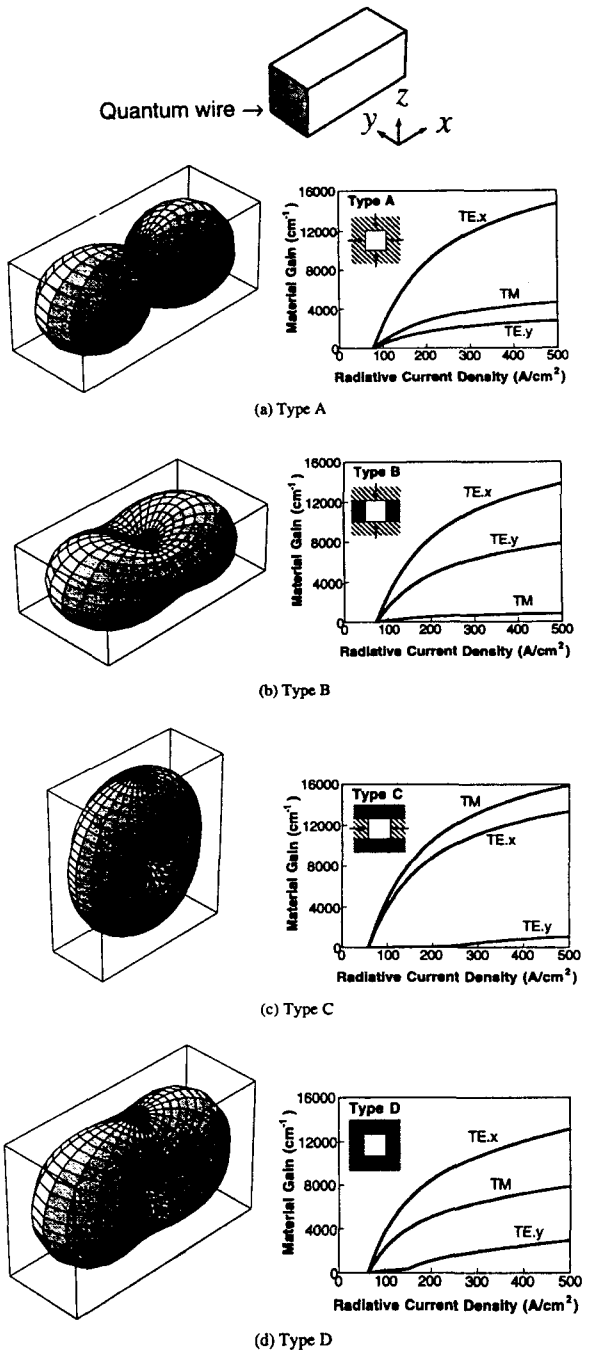

FIG. 5. Polarization dependence of optical gain in various types of quantum wire arrays. (Left side): the spherical plots of the dipole momentum matrix elements which are projected to the same perspective as in the diagram shown on the top. (Right side): the material gains for three polarizations along the x, y, and z axis which are denoted by TE.x, TE.y, and TM polarizations, respectively.

can expect a polarization independent optical amplification between two polarizations. On the other hand, the material gain for the TE.y polarization is almost negligible, thus one can expect a high extinction ratio between the TM and TE.y polarizations. The magnitudes of the dipole momentum matrix elements for three polarizations are summarized in Table 2.

V. OPTICAL GAIN

The maximum material gains as a function of the radiative current density in the various quantum wires are calculated [13] and plotted in Fig. 6(a). The variation of the threshold current density as a function of total cavity loss is also plotted in Fig. 6(b). They are also compared to those of the unstrained GaAs quantum wire array with the same lateral dimension [13]. The active volume is taken as the whole quantum wire array plane including the quantum wires and the barriers between them. Generally, the effective mass in the InGaAs is smaller than that of the GaAs hence the energy differences in the quantized states are larger in the InGaAs quantum wires than in the GaAs quantum wires for the same lateral dimension. Thus, the four types of InGaAs quantum wires have a higher optical gain than the GaAs quantum wires as shown

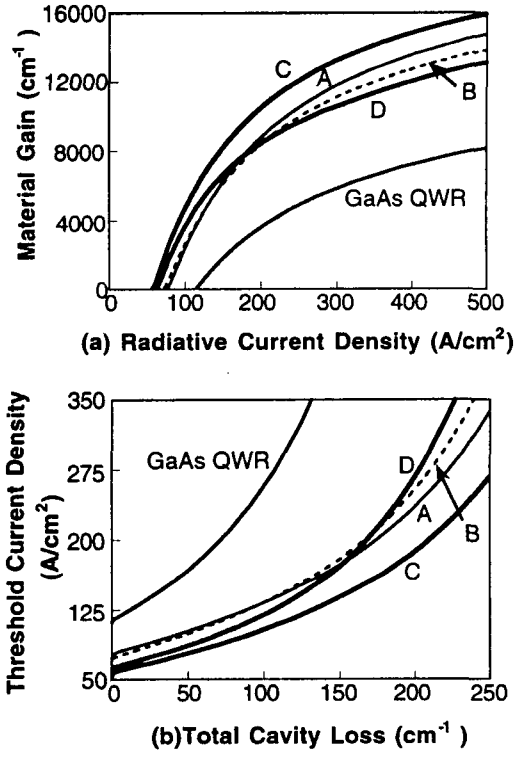

FIG. 6. (a) Variation of the material gain as a function of the radiative current density, and (b) variation of the threshold current density as a function of the total cavity loss in the strained (A-C) and unstrained (D) $In_{0.3}Ga_{0.7}As$ quantum wire arrays. Those of the $GaAs/Al_{0.5}Ga_{0.5}As$ with the same lateral dimension are also shown for a comparison.

in Fig. 6. Among the InGaAs quantum wires, type C strained quantum wire array has a higher optical gain than any other types of strained or unstrained quantum wire arrays. As seen from the band structure in Fig. 4, the large energy difference between the top valence subbands would contribute to obtaining the highest optical gain. When the energy splitting between the top valence subbands is smaller than 1 kT, the kinetic momentum of the holes from the different subbands would have a different value and is usually smaller than that of the electrons at the quasi-Fermi surface. The mismatch in the kinetic momentum between the holes and the electrons will reduce the radiative recombination due to the momentum conservation law. However, if the energy splitting between the top valence subbands is larger than 1 kT, the radiative recombination between the conduction band and the top valence subband will be greatly enhanced since the kinetic momentum of the electrons and holes at the quasi-fermi surfaces will be the same. This is why the larger valence subband splitting results in the enhanced optical gain. For types A and B quantum wire arrays, however, the optical gain is smaller than for type D unstrained quantum wire array due to the smaller valence subband splitting at the top. Consequently, the threshold current density for type A and B would be larger than that of type D. For instance, when the total cavity loss is 100 cm^{-1}, the threshold current densities are 103, 120, 130, and 132 A/cm^2 for the types C, D, A, and B quantum wire arrays, respectively. Thus certain types of strained quantum wires show larger or smaller threshold current densities than the unstrained quantum wire array. Therefore, the stress profile should be carefully chosen to enhance the optical gain in the strained quantum wire structures.

VI. CONCLUSIONS

In this paper, various types of strained quantum wire arrays are analyzed using the finite-element method [8,13]. The strain profile is rigorously calculated numerically including the hydrostatic and the shear strain components. The effect of the strain on the optical gain properties is quantitatively analyzed for various types of InAlGaAs quantum wire arrays. The polarization dependence of the optical gain turns out to be sensitive to the stress profile. Considering this phenomena, one can obtain a desirable optical anisotropy by controlling stress profiles, which can be exploited either for the single polarization optoelectronic devices or for the polarization independent devices.

ACKNOWLEDGEMENTS

This work is partly supported by 2001 Hong Ik University Academic Research Fund and Korea Nano-Photonics Projects 2002.

*Corresponding author : wave@hongik.ac.kr.

REFERENCES

[1] K. Y. Cheng, E. M. Stellini, P. J. Pearah, A. C. Chen, A. M. Moy, and K. C. Hsieh, International Electron Device Meeting '92(IEEE), 875 (1992).
[2] P. J. Pearah, E. M. Stellini, A. C. Chen, A. M. Moy, K. C. Hsieh, and K. Y. Cheng, Appl. Phys. Lett. **62**, 729 (1993).
[3] M. Walther, E. Kapon, C. Caneau, D. M. Hwang, and L. M. Schiavone, Appl. Phys. Lett. **62**, 2170 (1993).
[4] T. Yamauchi, T. Takahashi, and Y. Arakawa, Surface Science **267**, 291 (1992).
[5] J. C. Yi, N. Dagli, and L. A. Coldren, Appl. Phys. Lett. **59**, 3015 (1991).
[6] M. S. Miller, H. Weman, C. E. Pryor, M. Krishnamurthy, P. M. Petroff, H. Kroemer, and J. L. Merz, Phys. Rev. Lett. **68**, 3464 (1992).
[7] R. C. Miller, D. A. Kleinman, and A. C. Gossard, Phys. Rev. B **29**, 7085 (1984).
[8] J. C. Yi and J. B Ji, J. Optical Society of Korea, submitted (2002).
[9] J. C. Yi and N. Dagli, Inst. Phys. Conf. Series **145**, 943 (1995).
[10] G. E. Pikus and G. L. Bir, Sov. Phys.-Solid State **1**, 1502 (1960).
[11] G. E. Pikus and G. L. Bir, *Symmetry and strain-induced effects in semiconductors*, (Wiley, New York, 1974) Chapter 3.
[12] J. M. Luttinger and W. Kohn, Phys. Rev. **97**, 869 (1955).
[13] J. C. Yi and N. Dagli, IEEE J. Quantum Electron. **31**, 208 (1995).
[14] Landolt-Bornstein, *Numerical Data and Functional Relationships in Science and Technology*, (Springer, Berlin, 1982), vols. 17 and 22a.
[15] T. Yamauchi, T. Takahashi, and Y. Arakawa, Surface Science **267**, 291 (1992).
[16] C. Y. P. Chao and S. L. Chuang, Phys. Rev. B **46**, 4110 (1992).